IPEM Institute of Physics and Engineering in Medicine

**PAPER**

# Quantitative comparison of human myocardial fiber orientations derived from DTI and polarized light imaging

View the article online for updates and enhancements.

# Physics in Medicine & Biology

IPEM Institute of Physics and Engineering in Medicine

CrossMark

**PAPER**

# Quantitative comparison of human myocardial fiber orientations derived from DTI and polarized light imaging

Feng Yang[1,2,7], Yue-Min Zhu[2], Gabrielle Michalowicz[3,4], Pierre-Simon Jouk[3,4], Laurent Fanton[2,5], Magalie Viallon[2,6], Patrick Clarysse[2], Pierre Croisille[2,6] and Yves Usson[3]

[1] School of Computer and Information Technology, Beijing Jiaotong University, Beijing, People's Republic of China
[2] Univ Lyon, INSA-Lyon, Université Claude Bernard Lyon 1, UJM-Saint Etienne, CNRS, Inserm, CREATIS UMR 5220, U1206, F-69621, LYON, France
[3] Equipe DYCTIM, Laboratoire TIMC-IMAG, UMR5525 CNRS, Université Grenoble Alpes, La Tronche, France
[4] Centre Hospitalier Universitaire Grenoble Alpes, La Tronche, France
[5] Centre Hospitalier Universitaire Lyon, Lyon, France
[6] Centre Hospitalier Universitaire Saint-Etienne, Saint-Etienne, France
[7] Author to whom any correspondence should be addressed.

E-mail: fengyang@bjtu.edu.cn

## Abstract

Diffusion tensor imaging (DTI) is a non-invasive technique used to obtain the 3D fiber structure of whole human hearts, for both *in vivo* and *ex vivo* cases. However, by essence, DTI does not measure directly the orientations of myocardial fibers. In contrast, polarized light imaging (PLI) allows for physical measurements of fiber orientations, but only for *ex vivo* case. This work aims at quantitatively comparing the myocardial fiber orientations of whole human hearts obtained from cardiac DTI with those measured by PLI. Whole human neonatal and infant hearts were first imaged using DTI. The same whole hearts were then imaged using PLI. After DTI and PLI data are registered, the orientations of fibers from the two imaging modalities were finally quantitatively compared. The results show that DTI and PLI have similar variation patterns of elevation and azimuth angles, with some differences in transmural elevation angle range. DTI itself induces an underestimation of the range of transmural elevation angles by a factor of about 25° at the basal and equatorial slices and the reduction of spatial resolution further decreases this range. PLI data exhibit a $15° \pm 5°$ ($P < 0.01$) narrower transmural elevation angle range at apical slices than in basal or equatorial slices. This phenomenon is not observed in DTI data. In both modalities, the azimuth angle maps exhibit curved or twisting boundaries at the basal and apical slices. The experimental results globally enforce DTI as a valid imaging technique to reasonably characterize fiber orientations of the human heart noninvasively.
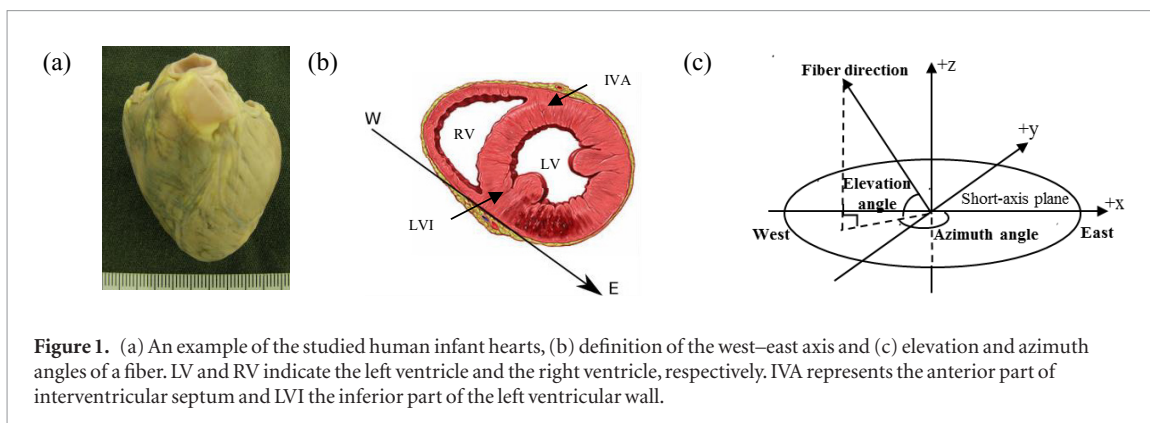
## Abbreviations used

DTI      Diffusion tensor imaging
PLI      Polarized light imaging
dMRI      diffusion magnetic resonance imaging
MDDW      Multi directional diffusion weighting
MMA      methacrylate
MRI      Magnetic resonance imaging
ADC      Apparent diffusion coefficient
FFD      Free form deformation
SSD      Sum of squared differences
FS      Finite strain
LV      Left ventricle
RV      Right ventricle
ODF      Orientation distributions functions
HARDI      high angular resolution diffusion-weighted imaging

## 1. Introduction

The myocardium is a complex tissue composed of various elements such as myocytes, collagen fibers, blood vessels, and other connective tissue elements (Caulfield and Borg 1979 and Weber 1989). Among these, myocytes play a central role in the cardiac contractile function. Since the myocytes have approximately 25 $\mu$m in diameter and 100 $\mu$m in length, current imaging systems (e.g. magnetic resonance imaging—MRI) do not enable to observe the individual myocytes of a whole myocardium. Instead, only an aggregate of individual myocytes is observed in an image voxel. Nevertheless, the myocyte aggregate is highly structured and oriented. When tracking the orientation of the myocyte aggregate at each voxel, the voxels form preferential patterns in three-dimensional (3D) space and give rise to the so-called myocardial fibers. Such fibers however should not be understood in the same sense as in brain or musculo-skeletal tissue, because they are actually the image representation of a set of individual myocytes having some privileged orientations in 3D space and the term 'fiber' is employed just for simplicity. Myocardial fibers have a fundamental role in the heart's function in health and disease (Weber 1989). For instance, the propagation of electrical activity is faster along the direction of the fibers and slower across the sheet plane (Jouk *et al* 2007), and at the cellular level, the contraction occurs along the long axis direction of the myocytes bundles and leads to transmural thickening and apex-base shortening after rearrangements through interactions with the collagen extracellular matrix. Moreover, fibers throughout the ventricles could be a substrate for arrhythmias, including ventricular tachycardia and fibrillation, and sudden cardiac death, as suggested in both experimental and theoretical studies (Collin 2006, Delon *et al* 2006, Wu *et al* 2006). A number of methods have been reported in the literature for the study of myocardial fiber architecture in a whole human heart. We can cite three main ones: histological techniques (Torrent-Guasp 1973, Ross and Streeter 1979, Streeter 1979), diffusion magnetic resonance imaging (dMRI) (Basser and Pierpaoli 2011 and Wu *et al* 2006), and polarized light imaging (PLI) (Usson *et al* 1994, Jouk *et al* 1995, 2000, 2007). Histological techniques are known to suffer from distortion and misalignment and do not allow the 3D reconstruction of fiber structures. To cope with these problems, PLI was proposed to get fiber orientations in *ex vivo* human hearts. Owing to its high spatial resolution ($90 \times 90 \times 500$ $\mu$m$^3$) and ability to measure physically the 3D orientations of the myocytes of a whole human heart, PLI appears a privileged technique for obtaining the ground-truth of the myocardial cell architecture of *ex vivo* human hearts (Whittaker *et al* 1989, Usson *et al* 1994, Jouk *et al* 2000). Indeed, PLI is founded on myosin orientation, a well-characterized component of the contractile apparatus constitutively coaxial with myocardial cells. However, PLI can only be applied to *ex vivo* hearts.

In contrast, dMRI can be used for both *ex vivo* and *in vivo* hearts, which makes it a novel promising imaging technique for both basic and clinical studies of cardiac diseases. dMRI produces diffusion-weighted (DW) images, by sensitizing magnetic resonance signals to the random motion (i.e. Brownian motion) of water molecules. The motion in the 3D space of water molecules can be free or hindered by obstacles, depending on their environment. In the case of the myocardium, the water molecules diffuse in a complex tissue structure but globally they move more rapidly in the direction where the structure has privileged orientations (e.g. fibrous structures), along the elongated direction of myocytes or bundles of myocytes (i.e. along the long-axis of the myocytes or myocardial fibers), and more slowly in the perpendicular direction. Water molecules then diffuse in an anisotropic manner in the myocardium. Capturing such 3D diffusion anisotropy will then enable to infer the fiber orientations of the tissue. To this end, magnetic field gradient pulses in different diffusion gradient directions (at least six) are used; each gradient direction accounts for water molecule displacement in that direction (Le Bihan 1991). When a sufficient number of diffusion gradient directions (>6) are used, diffusion tensor imaging (DTI) model (Basser *et al* 1994 and Kingsley 2006) provides an estimate of the main directions of diffusion. DTI has been shown to be an promising means to noninvasively image the fiber orientation of both *ex vivo* (Yang *et al* 2011, 2012, 2014, 2017, Eggen *et al* 2012, Lombaert *et al* 2012) and, more recently, *in vivo* human hearts (Wu *et al* 2006, Scott *et al* 2014, 2016, Wei *et al* 2015, McGill *et al* 2016, Moulin *et al* 2016).

However, DTI does not measure directly the orientations of myocardial fibers. Instead, it infers fiber orientations through tracking the motion of water molecules in the myocardium. The question then arises as to how the DTI-obtained fiber orientations reflect the reality. An attempt of answering this question was reported in Scollan *et al* (1998), Holmes *et al* (2000), Mekkaoui *et al* (2012) and Nielles-Vallespin *et al* (2017) on rabbit or sheep hearts using histological techniques. Scollan *et al* (1998) and Holmes *et al* (2000) compared the myofiber angulation at five corresponding locations from histology and DTI in rabbit hearts. Mekkaoui *et al* (2012) performed histological validation on six sections corresponding to six transmural depths in the lateral wall from endocardium to epicardium on 20 hearts of human, rat and sheep. Nielles-Vallespin *et al* (2017) compared the eigenvector angles from *in vivo* DTI and histology of a 1 cm $\times$ 1 cm block in the lateral left ventricle (LV) wall of the mid-ventricular level in swine hearts. More recent works on the evaluation of dMRI-derived fiber orientations in the human heart (Yang *et al* 2017) and in the human brains (Mollink *et al* 2017) were also reported, both of which take PLI as reference measures.

**Figure 1.** (a) An example of the studied human infant hearts, (b) definition of the west–east axis and (c) elevation and azimuth angles of a fiber. LV and RV indicate the left ventricle and the right ventricle, respectively. IVA represents the anterior part of interventricular septum and LVI the inferior part of the left ventricular wall.

With respect to our previous conference abstract (Yang *et al* 2017), in this paper, we propose to thoroughly and quantitatively compare the myocardial fiber orientations of whole human neonatal and infant hearts obtained from cardiac DTI with those measured by PLI. The method consists of first imaging the same whole human hearts using both DTI and PLI, then registering the DTI data to the PLI data, and finally comparing the fiber orientations of the whole hearts from both the imaging modalities. To the best of our knowledge, this is the first work to examine the whole-heart fiber orientations indirectly obtained from DTI with respect to those directly (physically) obtained from PLI, based on the imaging of the same whole human hearts.

## 2. Materials and methods

### 2.1. Human heart samples
In this study, nine human hearts were obtained and processed in compliance with French legal and ethical guidelines. The investigations are conformed to the principles outlined in the declaration of Helsinki (Anon n.d., Carlson *et al* 2004). They relate to infants who died after birth up to 14 months of life. After medically pronounced death, cadavers are conserved for a minimum of 24 h at the mortuary at 4 °C, in order to give time to the administration to verify there are no contra-indications to the necropsy and to the heirs of the deceased to give the authorization for the autopsy. Those legal formalities being done, the autopsy is performed; the heart are extracted and fixed in a formalin solution to ensure good preservation of cells and tissue as close as possible as living structure. The average weight of their ventricular masses ranged from 12 g to 32 g, and the average thickness of their interventricular septum at the equatorial level ranged from 3 to 8 mm. An example of the studied neonatal hearts is shown in figure 1.

The nine human neonatal and infant hearts were first imaged using DTI and then imaged using PLI.

### 2.2. Heart preparation and DTI
Each heart was placed in a plastic container and held by hydrophilic gel to maintain a diastolic shape. This setup has a low dielectric effect and also eliminates unwanted susceptibility artifacts near the boundaries of the heart. The DTI acquisitions of the nine *ex vivo* human neonatal and infant hearts were performed on a 3 T clinical scanner (MAGNETOM Verio, Siemens AG, Healthcare Sector, Erlangen, Germany). The 12 channels head matrix coil was used. The used DTI-sequence was a Siemens MDDW (Multi-Directional Diffusion Weighting) sequence with the following parameters: TE = 70 ms, TR = 5100–7900 ms, FOV = $144 \times 144$ mm$^2$, slice spacing = 1.4 mm, slice thickness = 1.4 mm, slice duration (average acquisition time for one slice) = 170–230 ms, number of slices = 30–40, size = $104 \times 104$ pixels, imaging voxel = $1.38 \times 1.38 \times 1.4$ mm$^3$, diffusion sensitivity $b = 700$ s mm$^{-2}$, gradient directions = 12, 32 or 192. For the 12 directions with ten averages (Heart 1) and 192 directions with 6 averages (for the other hearts), the acquisition times were 11.1 min and 148.7 to 177.7 min, respectively. Diffusion tensor calculation and analysis of fiber structure characteristics were carried out with MATLAB (The Mathworks Inc. 2016).

Although the present paper focuses on the comparison of fiber orientations derived from DTI and PLI, it would be useful to have some ideas on the values of fractional anisotropy (FA) and mean diffusivity (MD), two most popular DTI indices, obtained in the present study. Thus, the calculated mean FA and MD values and their standard deviations for the nine hearts were recorded in table 1.

### 2.3. Heart preparation and PLI
After DTI acquisitions, the nine hearts were imaged using PLI. The samples were rinsed in neutral buffer solution then immerged in a formalin solution to wait for PLI. The whole PLI imaging involves a series of operations that include in particular:

**Table 1.** DTI FA and MD mean and standard deviation values for the nine hearts.

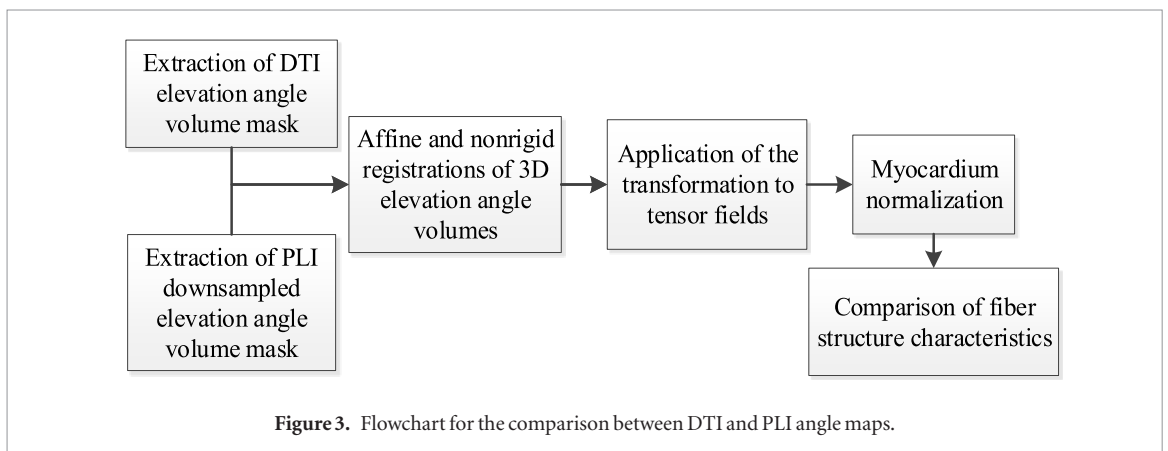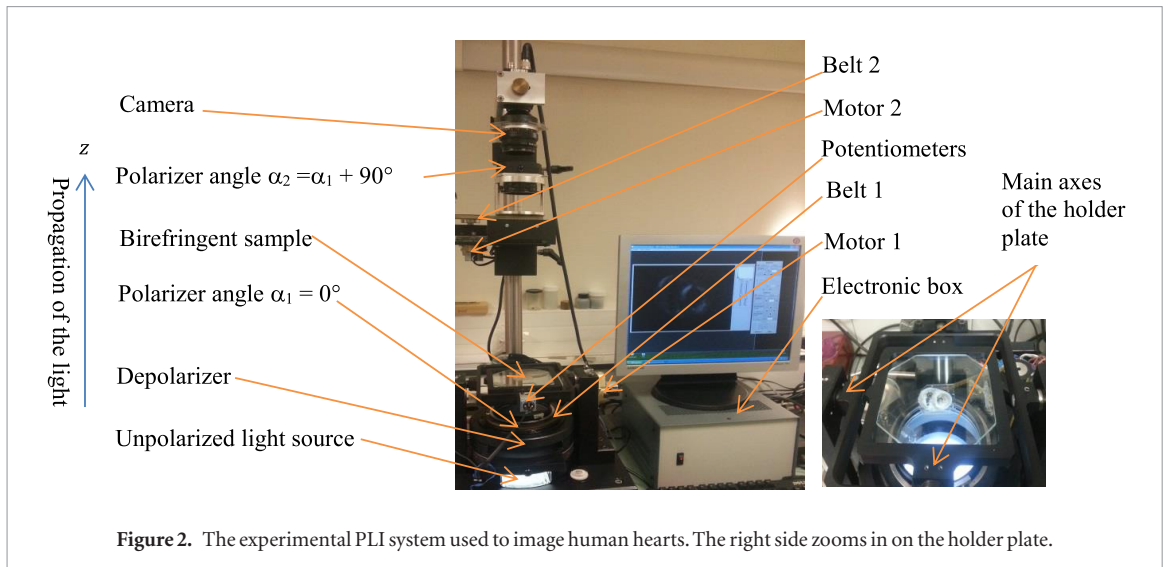|         | FA          | MD ($10^{-3}$ mm² s⁻¹) | Age        |
| ------- | ----------- | ----------------------- | ---------- |
| Heart 1 | 0.32 ± 0.17 | 0.61 ± 0.33             | 14 months  |
| Heart 2 | 0.13 ± 0.07 | 1.38 ± 0.40             | 2 months   |
| Heart 3 | 0.18 ± 0.06 | 1.40 ± 0.26             | 0          |
| Heart 4 | 0.32 ± 0.23 | 0.86 ± 0.55             | 2 months   |
| Heart 5 | 0.24 ± 0.10 | 1.22 ± 0.33             | 2 months   |
| Heart 6 | 0.23 ± 0.12 | 1.03 ± 0.41             | 8 d        |
| Heart 7 | 0.22 ± 0.11 | 0.82 ± 0.22             | 5 d        |
| Heart 8 | 0.36 ± 0.13 | 0.70 ± 0.21             | 2 d        |
| Heart 9 | 0.13 ± 0.07 | 1.32 ± 0.33             | 3 months   |
| Average | 0.24 ± 0.12 | 1.04 ± 0.34             | 2.61 months |

(a)  Tissue handling: the preserved heart samples were dissected and the ventricular masses were isolated by cutting the atria 1 mm upper from atrio-ventricular groove, and the great arteries 3 mm from the semi-lunar valves.

(b)  Embedding: The hearts (ventricular masses) were embedded in methyl methacrylate (MMA) resin using a protocol composed of eight successive baths (one week for each of them): one bath for eliminating formalin, four baths for dehydration, three baths for immersion in three different and successive solutions of MMA liquid resin. The samples were embedded in acrylic hard bocks resin by polymerization of the MMA. The chemical reactions took place in a controlled way and required one up to three weeks, to avoid shrinkage and production of artefacts.

(c)  Sectioning: before sectioning, three fiducial markers were drilled perpendicular to the coronal plane on the faces of the MMA resin block. A series of thick sections (thickness 500 $\mu$m) were cut with a diamond wire saw (ESCIL$^R$) in the heart short axis plane. Due to the thickness of the wire saw, 500 $\mu$m were lost and consequently the spacing of section was 1 mm. The rate of penetration of the saw was set at a low speed in order to avoid mechanical stress and distortions. Sectioning time was 30 to 45 min per section with 35 to 45 sections per heart.

(d)  PLI acquisition: The birefringence of the myocardium is essentially due to the crystalline uni-axial positive birefringence of myosin (Usson *et al* 1994, Jouk *et al* 1995, 2000, 2007)) and it is possible to cancel the intrinsic birefringence of collagen due to the good match of MMA and collagen refraction indices. The extraction of orientation information (Usson *et al* 1994, Jouk *et al* 2007) (in terms of elevation and azimuth angles) at each voxel ($90 \times 90 \times 500\ \mu$m³) is then possible with the classical technique of PLI on a 3-axis rotation stage adapted to biology, particularly at the low value of birefringence ($10^{-4}$) and the size of our specimen samples. The experimental PLI system is illustrated in figure 2. It consists of an optical bench with a polychromatic LED illuminator (White LED 5 W) source, a motorized rotating polarizer, a tiltable stage for holding the specimen, a motorized full wave plate (510 nm), a motorized rotating analyzer (crossed axis with reference to polarizer), a long-pass (590 nm) filter and a CCD camera. More details about heart preparation and imaging can be found in references (Jouk 1994, Jouk *et al* 1995, 2000, 2007). Each section requires recording 32 PLI images corresponding to various configurations of the optical pieces; each image requires an exposure time of half a second. The acquisition of each section lasted between 20 and 30 min or more, including the time for preliminary adjustments, setting of different filters, cleaning of artefacts such as blood clots, etc.

So, globally, about five to six months were needed to obtain the final elevation and azimuth maps of a single heart.

As mentioned above, the raw data provided by PLI are the values of elevation and azimuth angles physically measured by PLI in the reference system illustrated in figure 1. Therefore, we use elevation and azimuth angles in the following comparisons (instead of recalculating the helix and transverse angles under a cylindrical coordinate system).

### 2.4. Comparison scheme

The comparison scheme is illustrated in figure 3. It consists of five steps detailed in the following subsections. Since the raw data acquired by PLI and DTI represent different quantities (respectively fiber angle maps and DW images), their intensity values differ. Therefore, the myocardium masks of the same type of information from both modalities are generated. More precisely, elevation angle volumes from PLI and DTI are chosen as the mask for registration since the initially acquired PLI data are elevation and azimuth angles but the elevation angle map generally presents simpler variation pattern than azimuth angle map. To reduce registration computational cost,

**Figure 2.** The experimental PLI system used to image human hearts. The right side zooms in on the holder plate.



**Figure 3.** Flowchart for the comparison between DTI and PLI angle maps.

a reduction of the initial PLI volume size is performed by downsampling. The downsampling is in-plane with a downsampling factor of 4, which means that a $4 \times 4$ pixel array is replaced by a single value from a median filter.

### 2.4.1. Myocardium mask extraction

Due to the noisy nature of DTI data, the boundary between the myocardium and the fixation gel is not clear enough to be captured with a simple threshold-based segmentation of $b0$ images. We therefore extracted myocardium mask in the apparent diffusion coefficient (ADC) images that were calculated from the DW images. First, the ADC maps were thresholded using an upper threshold of $2 \times 10^{-3} \, \text{mm}^2 \, \text{s}^{-1}$, yielding the myocardium mask. Then, the myocardium in DTI elevation angle volume was extracted by the ADC myocardium mask. For the acquired PLI elevation angle volume, the papillary muscles were removed before registration for more accurate registration.

### 2.4.2. Affine and nonrigid registrations of DTI and PLI elevation angle volumes

Landmark-based 3D affine registration is first applied to cope with the problem in which the orientation of the same heart in the two imaging modalities differs a lot. Three landmarks at the equatorial slice and one landmark at the apical slice of LV are selected to reorient and resize the heart in both *x-y* plane and apex-base axis. After the affine registration, a bi-pyramidal free form deformation (FFD)-based registration (Sarrut *et al* 2007) is used to register the hearts in both modalities to the same shape. The affine and nonrigid registrations of DTI elevation angle volume to PLI elevation angle volume are schematized in figure 4. The term bi-pyramidal refers to the two multi-level pyramidal representations applied respectively to the images and the FFD transformation. The first pyramid achieves the multiresolution decomposition of the original images by applying independently a low-pass Gaussian filter to each of them and then decimating the number of voxels. The second pyramid realizes the multiresolution decomposition of the FFD transformation. The sum of squared differences (SSD) is used as the registration similarity criterion, and the optimization is achieved through a gradient descent search based on the first derivative of the SSD metrics (Sarrut *et al* 2007). In our experiments, the number of image pyramid levels and transformation pyramid levels were respectively set to 3 and 4.
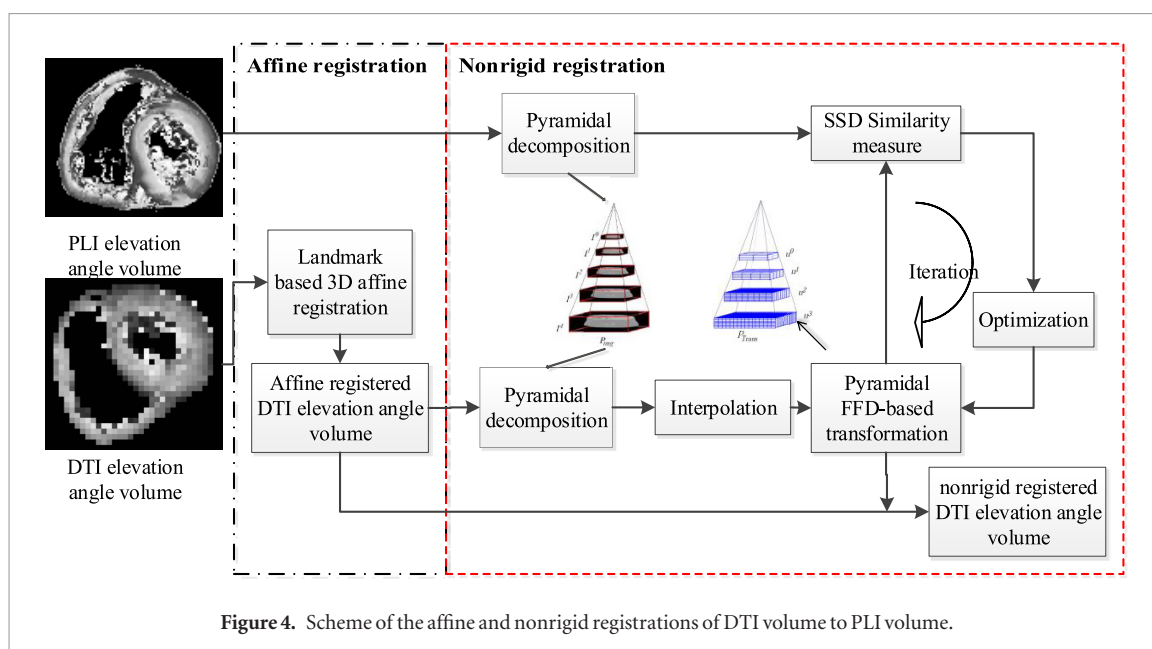
**Figure 4.** Scheme of the affine and nonrigid registrations of DTI volume to PLI volume.

### 2.4.3. Tensor field transformation and reorientation

By registering the DTI elevation angle volume to PLI elevation angle volume as described in Step ii), we obtain the affine and nonrigid transformations, which are then applied to the original tensor fields (that are calculated from DW images). That finally amounts to registering the original tensor fields to PLI data. The diffusion tensor at each voxel contains orientation information related to its local reference coordinate system, whereas the transformation refers to the relocation of each voxel in a global coordinate system. Therefore, a reorientation of the tensors based on the affine and nonrigid registrations must be performed to conserve the tensor size and shape in the image and to preserve the microstructure properties of tissues (Alexander *et al* 2001). In the present study, the finite strain (FS) strategy (Malvern 1969) was preferred since it preserves geometric features of diffusion tensors.

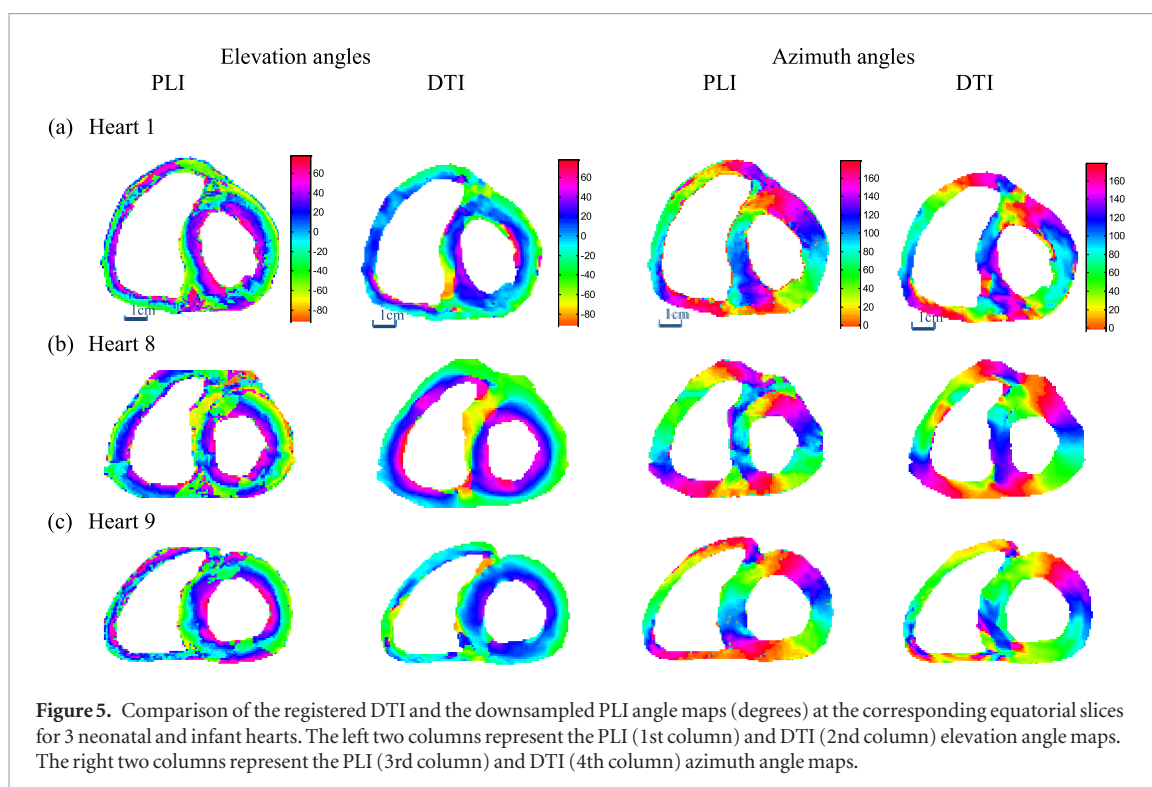### 2.4.4. Myocardium normalization

The normalization of myocardium is achieved for both elevation and azimuth angle maps derived from PLI and registered DTI tensor fields in the same coordinate system. The transmural position within myocardium is normalized in a manner similar to that in Geerts *et al* (2002) in order to redefine a common coordinate system and locate relative transmural positions in the myocardium. To achieve this, an estimated radius of the midwall position is first determined and then used as a reference radius to which all transmural positions are normalized.

### 2.4.5. Comparison of fiber structure characteristics

The comparison of fiber structure characteristics between DTI and PLI is based on the elevation and azimuth angle maps, transmural elevation angle distribution, transmural elevation angle range, and histogram of elevation angles. Note that papillary muscles are excluded for the quantitative comparison of elevation and azimuth angles and transmural elevation angle ranges, to focus on the fiber characteristics within the myocardial wall only. The transmural elevation angle range of the whole LV myocardium of a given slice is calculated by subtracting the mean elevation angle at free wall epicardium (or RV septum endocardium) from that at LV free wall endocardium (or LV septum endocardium).

## 3. Results

Figure 5 shows the comparison between the downsampled PLI angle map and the corresponding registered DTI angle map for three of the nine neonatal and infant hearts. Taking Heart 1 as an example, the left two columns in figure 5 represent the PLI and DTI elevation angle maps and the right two columns the PLI and DTI azimuth angle maps. The PLI angle maps were obtained after downsampling the original angle maps derived from the redirected vector fields of the equatorial slice in PLI, while the DTI angle maps were obtained from the non-rigidly registered tensor fields of the same slice in DTI. From the PLI maps, it is observed that most elevation angles in the LV myocardium (1st image, figure 5(a)) vary continuously from about $-60°$ to $+60°$ from epicardium to endocardium in the free wall or from RV septum endocardium to LV septum endocardium. The azimuth angle map (3rd image, figure 5(a)) exhibits a circularly periodic variation pattern in the LV myocardium, with a whole

**Figure 5.** Comparison of the registered DTI and the downsampled PLI angle maps (degrees) at the corresponding equatorial slices for 3 neonatal and infant hearts. The left two columns represent the PLI (1st column) and DTI (2nd column) elevation angle maps. The right two columns represent the PLI (3rd column) and DTI (4th column) azimuth angle maps.

range of angles (0°–180°) being experienced twice. The variations of both elevation and azimuth angles reflect the helical structure of cardiac fibers.
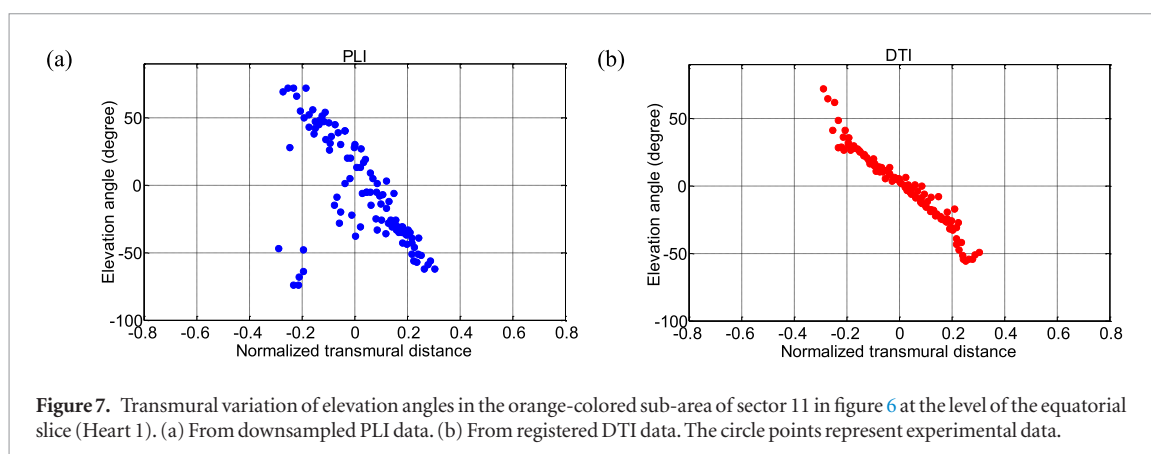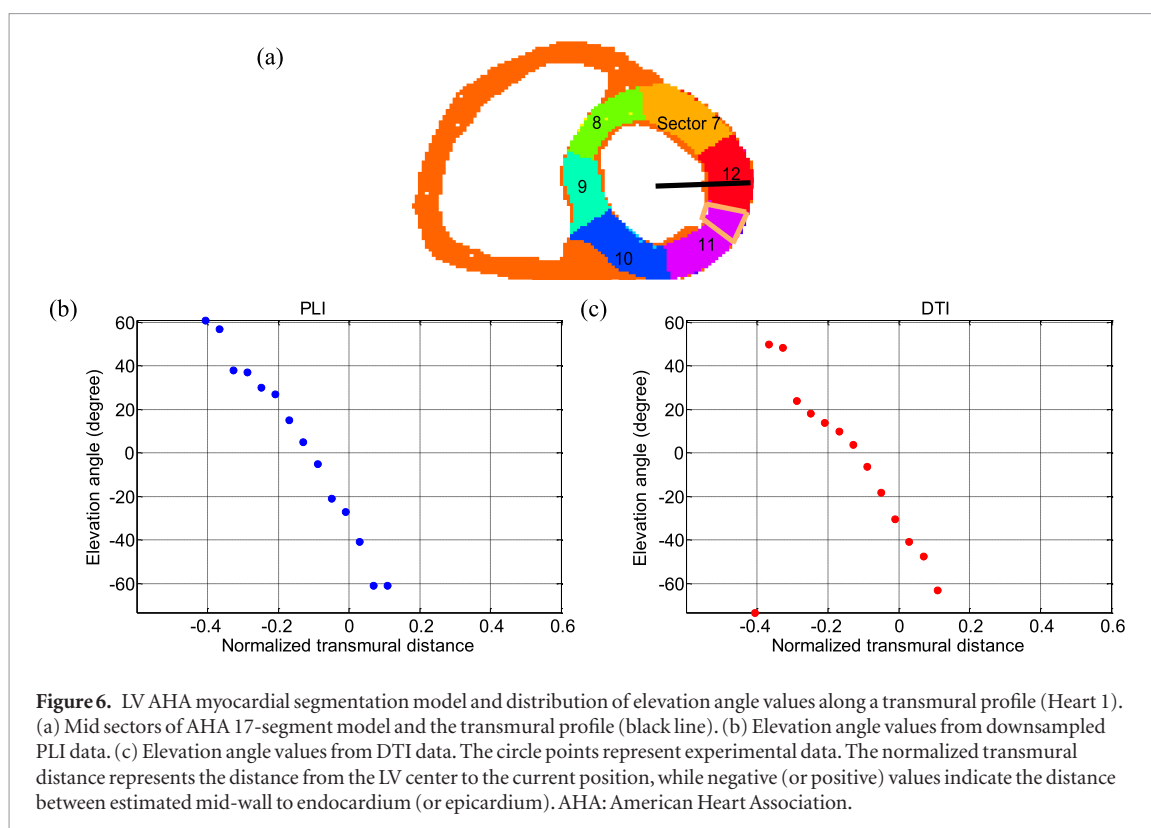
From the registered DTI (the 2nd and 4th images, figure 5(a)), we observe that the regular variation pattern of elevation and azimuth angles is preserved. However, the DTI elevation angle presents a reduced range of variations, varying from about −45° to +45° from epicardium to endocardium of the free wall or from RV septum endocardium to LV septum endocardium; the azimuth angle map presents a circularly periodic variation similar to that of the downsampled PLI, but with some singular values appearing in the IVA area (illustrated in figure 1(b)). Singular values in the angle maps from the registered DTI are observed along the RV septum endocardium and the LV endocardium, which correspond to residual papillary muscles; but they are much less numerous than those in the PLI angle maps. This is because the values of the DW signals of papillary muscles are close to those of gel, and have been discarded in the registration process. In the following comparison based on registration, Heart 1 was again taken as a representative example.

Figure 6 shows the distribution of elevation angles along a radial profile (Heart 1) at an equatorial slice (figure 6(a)) from downsampled PLI data (figure 6(b)) and registered DTI data (figure 6(c)). It is observed that along this profile the elevation angles vary from −60° to +60° in downsampled PLI data (figure 6(b)) and from −65° to +50° in registered DTI data (figure 6(c)).

Figure 7 gives the distribution of elevation angles in the orange-delimited sub-area of Sector 11 (figure 6(a)) for downsampled PLI and registered DTI data. The elevation angle varies from positive to negative values when going from endocardium to epicardium of the free wall or from LV septum endocardium to RV septum endocardium. More singular elevation angle values are observed at the endocardium in PLI than in registered DTI, due to the presence of residual papillary muscles in PLI data.

In a more global manner, figure 8 shows the histograms of elevation angles at all pixels at basal, equatorial and apical slices. Clearly, the elevation angle histogram of PLI is much broader than that of DTI. The elevation angle histograms of both PLI and DTI exhibit coarsely a bimodal shape. Near the zero elevation angle, there is a rather abrupt change in amplitude of the histograms. It seems that the zero elevation angle value separates the histogram into two parts. For the three slices, the main energy of the PLI histogram is concentrated between the elevation angles −60° and +60° whereas that of the DTI histogram between −30° and +30°.

The experiments on the nine neonatal and infant hearts showed similar results on both elevation and azimuth angles. To more clearly compare the difference of the nine hearts for the two modalities and different resolutions, the transmural elevation angle ranges of the LV myocardium at basal, equatorial and apical slices for all the nine hearts are illustrated in figures 9(a)–(c) by box-and-whisker plots. The original DTI shows an obvious reduction ($85° \pm 11°$, $p < 0.001$ at the basal and equatorial slices) in the transmural elevation angle range, compared to the original PLI. The registered DTI exhibits, at the basal and equatorial slices, a transmural elevation angle range about 25° ($25° \pm 14°$, $p < 0.005$) smaller than that of the downsampled PLI that in turn presents a decrease of about 35° ($35° \pm 6°$, $p < 0.001$) with respect to the original PLI. The transmural elevation

**Figure 6.** LV AHA myocardial segmentation model and distribution of elevation angle values along a transmural profile (Heart 1). (a) Mid sectors of AHA 17-segment model and the transmural profile (black line). (b) Elevation angle values from downsampled PLI data. (c) Elevation angle values from DTI data. The circle points represent experimental data. The normalized transmural distance represents the distance from the LV center to the current position, while negative (or positive) values indicate the distance between estimated mid-wall to endocardium (or epicardium). AHA: American Heart Association.



**Figure 7.** Transmural variation of elevation angles in the orange-colored sub-area of sector 11 in figure 6 at the level of the equatorial slice (Heart 1). (a) From downsampled PLI data. (b) From registered DTI data. The circle points represent experimental data.

angle range is significantly smaller at the apical slice than at the basal or equatorial slice in both the original PLI ($15° \pm 5°$, $p < 0.01$) and the downsampled PLI ($19° \pm 13°$, $p < 0.05$). Significant differences between apical and basal (or equatorial) slices were observed neither in the original DTI nor in the registered DTI within the nine hearts. Since the azimuth angle range remains very close at different slices, we illustrate in figure 9(d) the average azimuth angle range of basal, equatorial and apical slices for the nine hearts. The original PLI keeps an azimuth angle range of $179°$, while the original DTI, the downsampled PLI and the registered DTI exhibit an azimuth angle range around $178°$.

Concerning azimuth angle characteristics, all the nine hearts exhibit boundaries (defined as borders between two colored regions in figure 10) in their azimuth angle maps derived from both DTI and PLI. In all the nine PLI azimuth angle maps, the boundaries are parallel to the rays from the LV center at equatorial slices, but present a clockwise twisting at basal slices and counter clockwise twisting at apical slices (figure 10(a)). Similar curved or twisting boundaries in the azimuth angle maps at basal and apical slices are observed in DTI (figure 10(b)) of the nine hearts, but less regular as compared to PLI.

## 4. Discussion

Similar variation patterns of elevation and azimuth angles were globally observed in both DTI and PLI. However, some differences are observed between the measurements from these two imaging modalities. Compared to the original PLI, the original DTI exhibits substantially reduced transmural elevation angle range. Also,
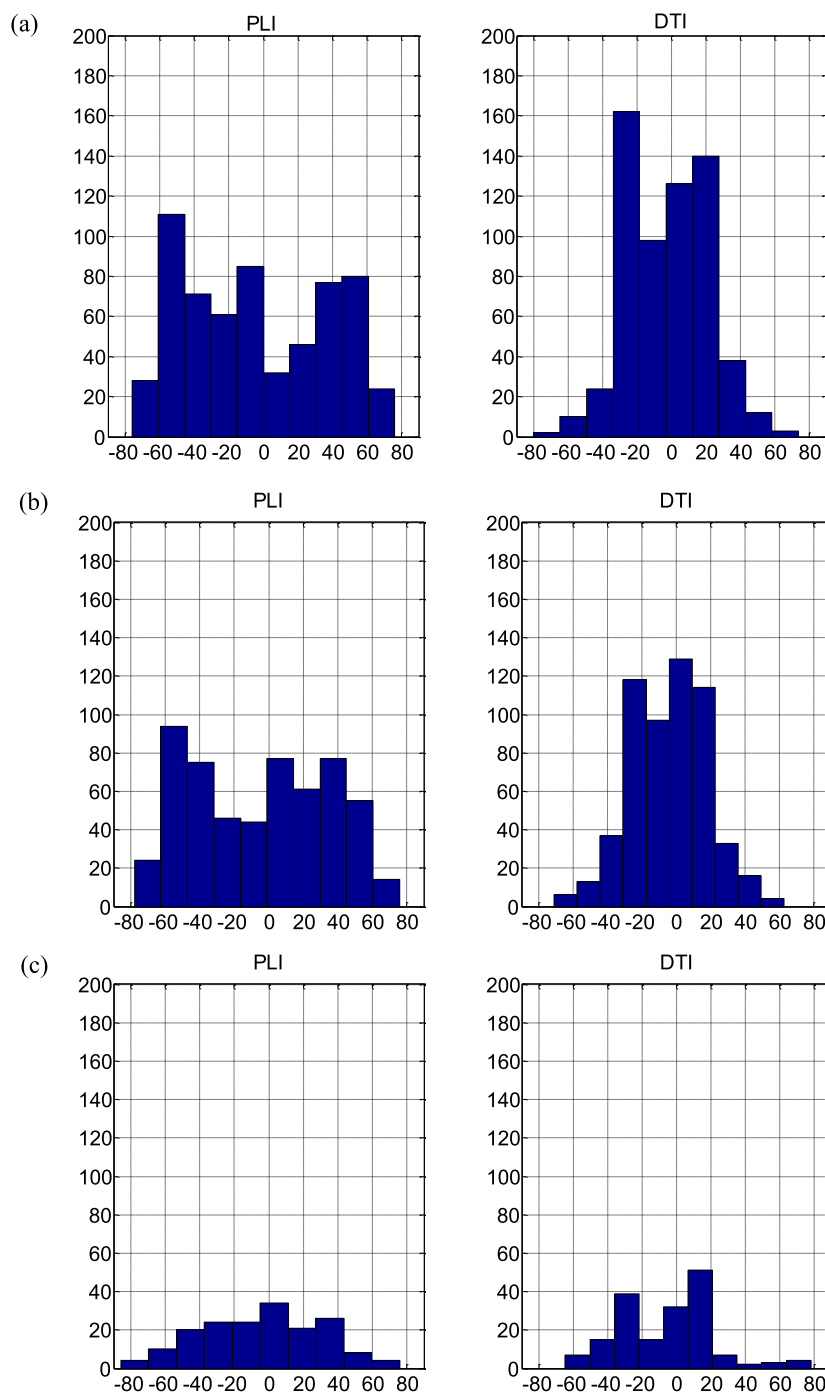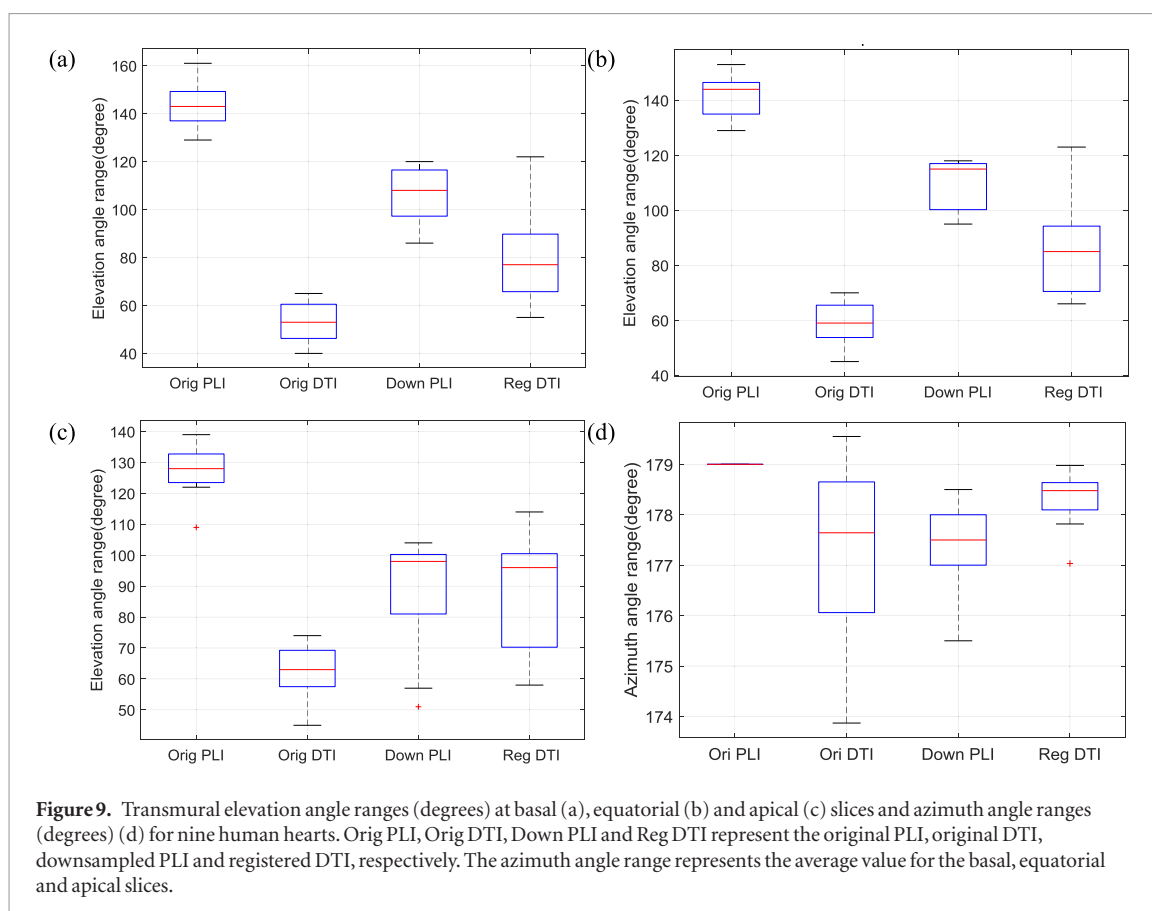
**Figure 8.** Elevation angle histograms of downsampled PLI (left column) and registered DTI (right column) at basal (a), equatorial (b) and apical (c) slices (Heart 1).

elevation angle range is influenced by segmentation and/or registration involved in quantitative comparison. In contrast, the azimuth angle range remains almost unchanged whatever the imaging modality or processing (downsampling and registration) performed.

### 4.1. Influence of registration

As observed in the above results, registration has widened the range of transmural elevation angles. This can be explained as follows. The involved DTI registration is a relatively complex nonlinear process that aims to register the low-resolution DTI data to the high-resolution PLI data. In such nonlinear process are involved a few operations such as interpolation. After such nonlinear process, the original DTI is registered to the downsampled PLI, with the consequence that the registration produces at the same time the effect of increasing the low-resolution of the original DTI data roughly to the higher-resolution of the downsampled PLI data. In other words, the involved registration reconstructs by essence a new high-resolution DTI data that have comparable

**Figure 9.** Transmural elevation angle ranges (degrees) at basal (a), equatorial (b) and apical (c) slices and azimuth angle ranges (degrees) (d) for nine human hearts. Orig PLI, Orig DTI, Down PLI and Reg DTI represent the original PLI, original DTI, downsampled PLI and registered DTI, respectively. The azimuth angle range represents the average value for the basal, equatorial and apical slices.

resolution to that of the downsampled PLI. Such increase in spatial resolution of the registered DTI would be mostly responsible for the widening of its elevation angle range. Note that the spatial resolution increase was not simply due to the involved interpolation. This is because simple interpolation alone does not allow for the improvement of the spatial resolution.

In addition to the fact that registration widens the transmural elevation angle range as just mentioned above, registration also has the effect of smoothing local variations of elevation angles, due to the involved interpolation.

In the present study, the elevation angle maps were chosen as the mask for registration instead of b0 (i.e. $b = 0$ or not DW) or trace (the average of the three eigenvalues of the diffusion tensor) images that are often used in DTI registration. This approach has been taken because no corresponding $b0$ or trace images exist in PLI.

### 4.2. Reduction of transmural elevation angle range

When passing from high spatial resolution to lower spatial resolution, the transmural elevation angle range of the downsampled PLI was reduced by about 35° in average (under the downsampling factor 4), as compared to the original PLI. Such reduction is obviously caused by the decrease in spatial resolution of downsampled PLI with respect to the original PLI.

A net reduction of transmural elevation angle range was observed in registered DTI with the downsampled PLI as the reference (25° ± 14°). These two sets of data are comparable in the sense that they have been aligned and can be considered in anatomical correspondence. The reduction of 25° in average is perhaps due to the DTI itself. In fact, the reduction caused by (original) DTI itself is even greater than 25°, because the registered DTI has widened the transmural elevation angle range with respect to the original DTI due to the spatial resolution increase.

### 4.3. Influence of papillary muscles

The presence of residual papillary muscles after segmentation of the images generated outliers in elevation angle maps, which can artificially increase the range of elevation angles. Our experiments showed that, after removing the outliers, a decrease of 6° ± 1° and 14° ± 8° on the transmural elevation angle range was observed respectively for original PLI and original DTI, and about 15° ± 4° and 13° ± 4° decreases respectively for downsampled PLI and registered DTI. The relatively small difference (6° ± 1°) between with and without removing outliers in original PLI is due to the fact that original PLI has a much higher spatial resolution with very smooth transitions at epi- and endocardial borders. As a result, removing one or two pixels will not induce a great change on the angle distributions. In contrast, abrupt variation of elevation angles between neighboring pixels was observed

for original DTI that has a much lower resolution (about one twentieth of the original PLI, with less than 10 pixels transmurally).

### 4.4. Twisting boundary of azimuth angles

By comparing the variations in azimuth angle at different slice levels from both DTI and PLI, we observed that the circular visiting pattern of azimuth angles was very similar from basal to apical slices including equatorial slice, except that the twisting of the boundaries diminished when going from the basal or apical slice to the equatorial slice. This is due to the fact that the parallel or twisting boundary reflects the 2D projection characteristic of the 3D helical structure of fibers.

### 4.5. Characterization of azimuth angle maps

We observe that the variation of azimuth angle ranges is on the order of a few degrees while the variation of elevation angle ranges is on the order of several tens of degrees. In other words, the difference in azimuth angle range between DTI and PLI is small. Such small difference in azimuth angle range however does not allow us to conclude that the azimuth angle map of DTI is the same as that of PLI. Indeed, difference between DTI and PLI azimuth angle maps is clearly visible in figures 5 and 10. That can be explained by the fact that, as a global quantitative metric, the azimuth angle range can only describe some limited characteristics of azimuth angle maps. Then, the question raises how to quantify in a pertinent manner the characteristics of azimuth angle maps of the myocardium. To our knowledge, there is still no standard metric for characterizing azimuth angle maps, the azimuth angle range we used being one metric among other possible ones. Further study on this issue may be worth pursuing.

### 4.6. Influence of formalin fixation

Previous results on animals (rats) suggest that cardiac tissues preserved in formalin prior to DTI imaging clearly showed an increase in water diffusivity and a decrease in the anisotropy degree, but there is some concern about the change in myocyte orientation. Indeed, Gilbert *et al* found that there is a low sensitivity of DTI-derived myocardial orientations in a rat to time post-fixation (Gilbert *et al* 2013), while, always on rats, Giannakidis *et al* showed that the cardiac tissue immersion in formalin caused the loss of the primary water diffusion orientation integrity in terms of the inter-voxel diffusion coherence index (IVDC) (Giannakidis *et al* 2016). Nevertheless, both the studies led to the same finding that the formalin fixation did not change the classic transmural variation of helical angles, from negative values at the epicardium to zero degree at the mesocardium (or midmyocardium) to positive values at the endocardium. Both our DTI and PLI results further confirmed that formalin fixation does not hamper the property of such helical angle transmural variation. Furthermore, since orientation from PLI represents the mean value of the orientations of all myosin filaments contained in a pixel while the myosin filaments are not degraded by formalin (Jouk 1994), that implies that the reduction in transmural elevation angle range observed in DTI really exists with respect to PLI. We (and other prior works) were however not able to determine whether such reduction is due to DTI itself or to formalin (or even to both of them) since we had not, for the same hearts, experimented with different formalin immersion durations. Also, we are not able to determine whether such reduction is due to noise or anything else because it concerns real cardiac tissues and we do not know the ground-truth.

### 4.7. Correlation between FA, MD and age

FA and MD are two different DTI indices that represent different aspects of the same phenomenon. FA is more related to the notion of 'direction' while MD reflects more the notion of 'extent, intensity, fluency'. In principle, we cannot establish any theoretical correlation between them because FA and MD are affected not only by tissue microstructure (which is highly complex and variable in the case of myocardium) but also by acquisition parameters (Barrio-Arranz *et al* 2015). Nevertheless, for our experimental results (table 1), by reporting the FA and MD values on the same plot, we observed a negative correlation between FA and MD values (correlation coefficient $= -0.87$) for the nine hearts. Concerning the correlation between FA (or MD) and age, by reporting FA (or MD) and age values on the same plot, we did not find any obvious relationship between them (correlation coefficients for FA versus Age and MD versus Age were 0.26 and $-0.42$, respectively).

### 4.8. Difference between ex vivo and *in vivo* cardiac DTI

The main difference between *ex vivo* and *in vivo* cardiac DTI is that we need not to consider motion effects (respiratory and cardiac motions) during *ex vivo* cardiac DTI. As a result, in *ex vivo* cardiac DTI, we can have higher SNR, better spatial resolution and no artifacts, which leads to wider helix angle ranges with respect to *in vivo* cardiac DTI (Nielles-Vallespin *et al* 2013, Toussaint *et al* 2013, Wei *et al* 2015). In addition, the fact that *in vivo* data are acquired at different cardiac phases may make it difficult to compare *ex vivo* and *in vivo* cardiac DTI in an accurate manner. Finally, in the present study, we used elevation angle (in order to compare with PLI) while
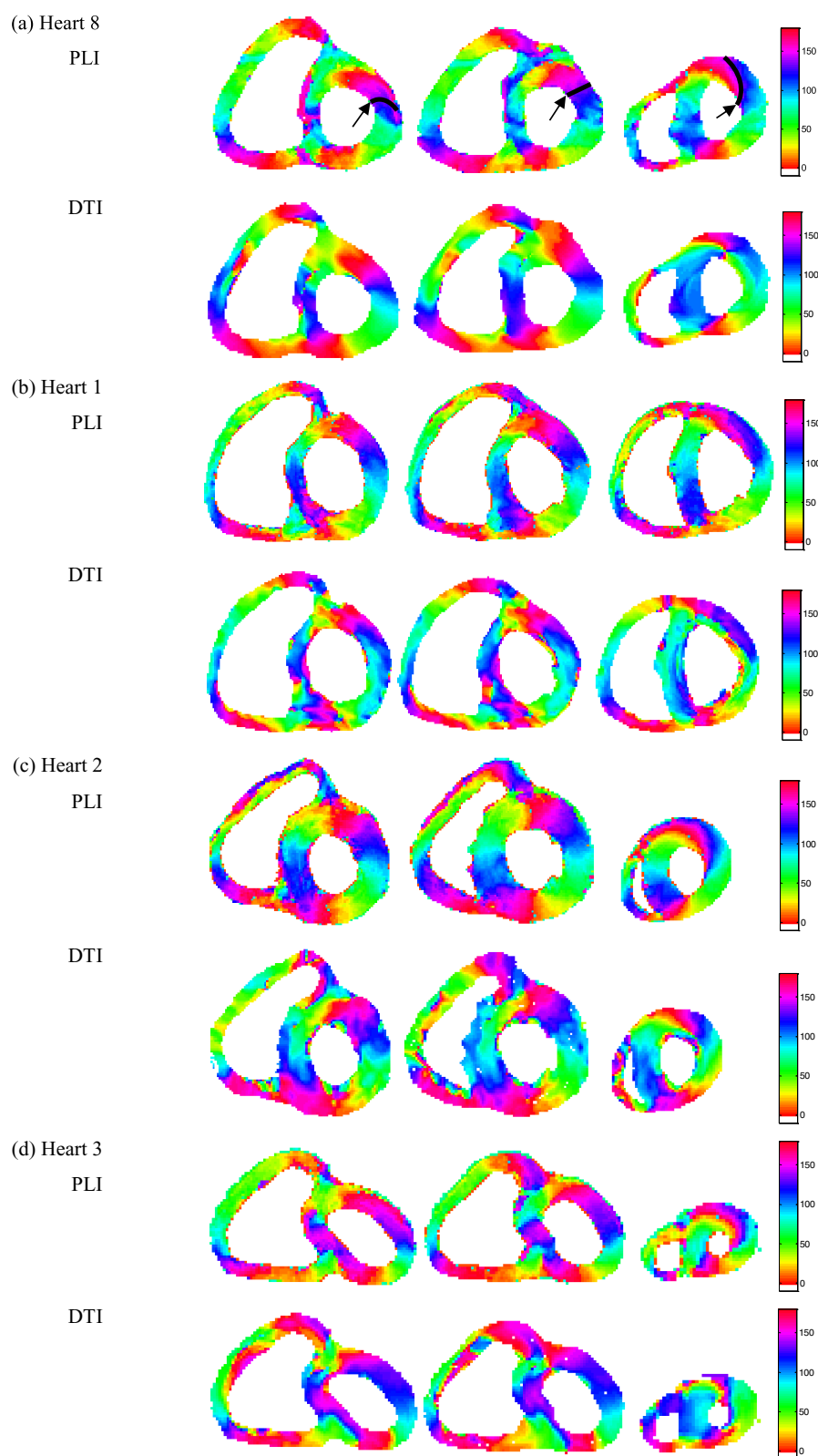
**Figure 10.** Azimuth angle maps of the nine hearts at the basal slice (left column), equatorial slice (middle column) and apical slice (right column) from downsampled PLI data (a) and registered DTI data (b). The thick black line or curves in (a) indicate the angle boundaries.

in existing *in vivo* cardiac DTI, the results were expressed in terms of helix angle. So, to be able to compare the fiber orientations obtained in the present *ex vivo* cardiac DTI with those of *in vivo* cardiac DTI, we first need to do conversions between the elevation angle-azimuth angle system and the helix angle-transverse angle system. This may be an interesting topic of further investigation.
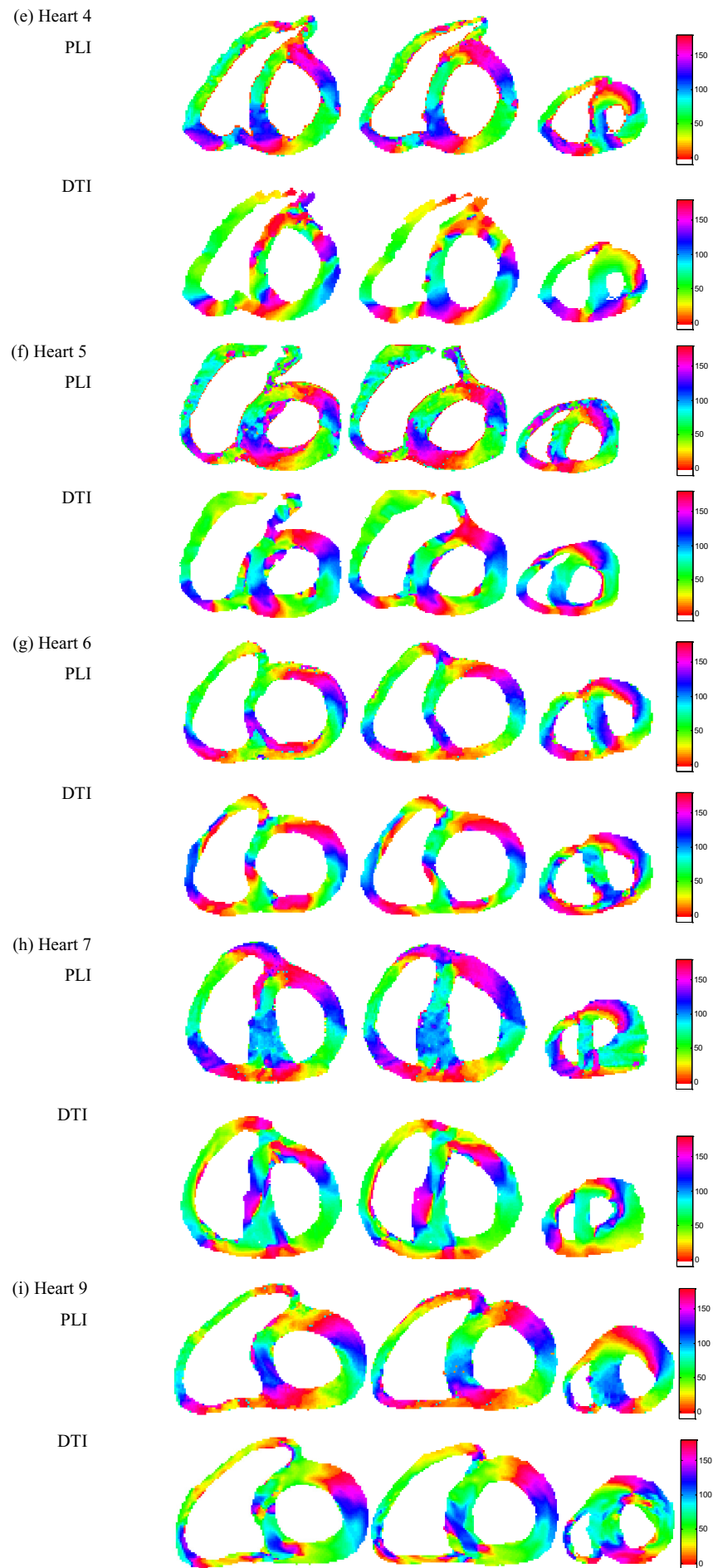
**Figure 10.** (*Continued*)

A last but very interesting point is related to the finding of Giannakidis *et al* on rodents (Giannakidis *et al* 2016), which demonstrates that the prolonged exposure to fixative resulted in a flatter probability density of helical angles with heavier tails. In reality, their helical angle probability densities, flatter or not, always exhibit a bimodal shape, namely they have two peaks, between which there is a valley near zero degree. Our results on human hearts appear comparable to this finding on rat hearts. Indeed, all our elevation angle histograms (equivalent to probability density for discrete case) from both DTI and PLI exhibit a bimodal shape. All these findings demonstrate that one of the most pertinent features of myocardial tissues (for human or animals) would be the bimodal shape distributions of their elevation or helical angle maps.

In conclusion, we have performed a thorough and quantitative comparison of DTI-derived and PLI-derived fiber orientations in human neonatal and infant hearts. Similar variation patterns of elevation and azimuth angles were found in DTI and PLI, but clear differences in transmural elevation angle range were observed. In particular, DTI introduced an underestimation of about $25° \pm 8°$ in average in transmural elevation angle range at the basal and equatorial slices. The reduction of spatial resolution also decreased the transmural elevation angle range. PLI data exhibited a $15° \pm 5°$ ($P < 0.01$) narrower transmural elevation angle range at apical slices as compared to basal and equatorial slices. This phenomenon was not found in DTI data. Both modalities showed that their azimuth angle maps have twisting boundaries at the basal and apical slices. This study globally enforces DTI as a valid imaging technique to reasonably characterize fiber orientations of the human heart non-invasively while showing that the imaging modality causes obvious underestimation of transmural elevation angle range and the disappearance of some features in azimuth angle maps. In addition, the framework proposed in this work can be applied to investigate the brain fiber microstructure such as fiber crossing by comparing PLI data with orientation distributions functions (ODFs) (Axer *et al* 2016) in high angular resolution DW imaging (HARDI). In the present study, we have used the elevation angle range and the azimuth angle range as metrics to analyze and characterize the elevation and azimuth angle maps of the myocardium. In the future, it would be interesting to seek for other metrics to more adequately characterize individual myocardial fiber arrangements.

## Acknowledgement

## ORCID iDs

Feng Yang ● https://orcid.org/0000-0002-8334-7450
Yue-Min Zhu ● https://orcid.org/0000-0001-6814-1449
Pierre-Simon Jouk ● https://orcid.org/0000-0001-8301-320X
Patrick Clarysse ● https://orcid.org/0000-0002-5495-7655

## References

Alexander D C, Pierpaoli C, Basser P J and Gee J C 2001 Spatial transformations of diffusion tensor magnetic resonance images *IEEE Trans. Med. Imaging* **20** 1131–9

Axer M, Strohmer S, Gräßel D, Bücker O, Dohmen M, Reckfort J, Zilles K and Amunts K 2016 Estimating fiber orientation distribution functions in 3D-polarized light imaging *Front. Neuroanat.* **10** 40

Barrio-Arranz G, de Luis-García R, Tristán-Vega A, Martín-Fernández M and Aja-Fernández S 2015 Impact of MR acquisition parameters on DTI scalar indexes: a tractography based approach *PLoS One* **10** e0137905

Basser P J and Pierpaoli C 2011 Microstructural and physiological features of tissues elucidated by quantitative-diffusion-tensor MRI *J. Magn. Reson.* **213** 560–70

Basser P J, Mattiello J and Lebihan D 1994 Estimation of the effective self-diffusion tensor from the NMR spin echo *J. Magn. Reson.* B **103** 247–54

Carlson R V, Boyd K M and Webb D J 2004 The revision of the declaration of Helsinki: past, present and future *Br. J. Clin. Pharmacol.* **57** 695–713

Caulfield J B and Borg T K 1979 The collagen network of the heart *Lab. Invest.* **40** 364–72

Collin O 2006 Spatiotemporal dynamics of actin-rich adhesion microdomains: influence of substrate flexibility *J. Cell Sci.* **119** 1914–25

Delon A, Usson Y, Derouard J, Biben T and Souchier C 2006 Continuous photobleaching in vesicles and living cells: a measure of diffusion and compartmentation *Biophys. J.* **90** 2548–62

Eggen M D, Swingen C M and Iaizzo P A 2012 *Ex vivo* diffusion tensor MRI of human hearts: relative effects of specimen decomposition *Magn. Reson. Med.* **67** 1703–9

Geerts L, Bovendeerd P, Nicolay K and Arts T 2002 Characterization of the normal cardiac myofiber field in goat measured with MR-diffusion tensor imaging *Am. J. Physiol. Heart Circ. Physiol.* **283** H139–45

Giannakidis A, Gullberg G T, Pennell D J and Firmin D N 2016 Value of formalin fixation for the prolonged preservation of rodent myocardial microanatomical organization: evidence by MR diffusion tensor imaging *Anat. Rec.* **299** 878–87

Gilbert S H, Smaill B H, Walton R D, Trew M L and Bernus O 2013 DT-MRI measurement of myolaminar structure: accuracy and sensitivity to time post-fixation, b-value and number of directions *Proc. of the Annual Int. Conf. of the IEEE Engineering in Medicine and Biology Society, EMBS* pp 699–702

Holmes A A, Scollan D F and Winslow R L 2000 Direct histological validation of diffusion tensor MRI in formaldehyde-fixed myocardium *Magn. Reson. Med.* **44** 157–61

Jouk P S 1994 Etude de la topographie des cellules myocardiques au cours du développement embryonnaire et fœtal *PhD thesis* Université de Grenoble 1, Saint-Martin-d'Hères, FRANCE

Jouk P S, Mourad A, Milisic V, Michalowicz G, Raoult A, Caillerie D and Usson Y 2007 Analysis of the fiber architecture of the heart by quantitative polarized light microscopy. Accuracy, limitations and contribution to the study of the fiber architecture of the ventricles during fetal and neonatal life *Eur. J. Cardiothorac. Surg.* **31** 915–21

Jouk P S, Usson Y, Michalowicz G and Grossi L 2000 Three-dimensional cartography of the pattern of the myofibres in the second trimester fetal human heart *Anat. Embryol.* **202** 103–18

Jouk P, Usson Y, Michalowicz G and Parazza F 1995 Mapping of the orientation of myocardial cells by means of polarized light and confocal scanning laser microscopy *Microsc. Res. Tech.* **30** 480–90

Kingsley P B 2006 Introduction to diffusion tensor imaging mathematics: series Part I–III *Concepts Magn. Reson.* A **28** 101–79

Le Bihan D 1991 Molecular diffusion nuclear magnetic resonance imaging *Magn. Reson.* Q **7** 1–30

Lombaert H, Peyrat J M, Croisille P, Rapacchi S, Fanton L, Cheriet F, Clarysse P, Magnin I, Delingette H and Ayache N 2012 Human atlas of the cardiac fiber architecture: Study on a healthy population *IEEE Trans. Med. Imaging* **31** 1436–47

Malvern L E 1969 *Introduction to the Mechanics of a Continuous Medium* (New Jersey: Prentice-Hall, Englewood Cliffs)

McGill L A, Ferreira P F, Scott A D, Nielles-Vallespin S, Giannakidis A, Kilner P J, Gatehouse P D, de Silva R, Firmin D N and Pennell D J 2016 Relationship between cardiac diffusion tensor imaging parameters and anthropometrics in healthy volunteers *J. Cardiovasc. Magn. Reson.* **18** 2

Mekkaoui C *et al* 2012 Fiber architecture in remodeled myocardium revealed with a quantitative diffusion CMR tractography framework and histological validation *J. Cardiovasc. Magn. Reson.* **14** 70

Mollink J *et al* 2017 Evaluating fibre orientation dispersion in white matter: comparison of diffusion MRI, histology and polarized light imaging *Neuroimage* **157** 561–74

Moulin K, Croisille P, Feiweier T, Delattre B M, Wei H, Robert B, Beuf O and Viallon M 2016 *In vivo* free-breathing DTI and IVIM of the whole human heart using a real-time slice-followed SE-EPI navigator-based sequence: a reproducibility study in healthy volunteers *Magn. Reson. Med.* **76** 70–82

Nielles-Vallespin S *et al* 2013 *In vivo* diffusion tensor MRI of the human heart: Reproducibility of breath-hold and navigator-based approaches *Magn. Reson. Med.* **70** 454–65

Nielles-Vallespin S *et al* 2017 Assessment of myocardial microstructural dynamics by *in vivo* diffusion tensor cardiac magnetic resonance *J. Am. Coll. Cardiol.* **69** 661–76

Ross A and Streeter D 1979 Myocardial fiber disarray *Circulation* **60** 1425–6

Sarrut D, Delhay B, Villard P, Boldea V, Beuve M and Clarysse P 2007 A comparison framework for breathing motion estimation methods from 4D imaging *IEEE Trans. Med. Imaging* **26** 1636–48

Scollan D F, Holmes A, Winslow R and Forder J 1998 Histological validation of myocardial microstructure obtained from diffusion tensor magnetic resonance imaging *Am. J. Physiol.* **275** H2308–18

Scott A D, Ferreira P F A D C, Nielles-Vallespin S, Gatehouse P, McGill L-A, Kilner P, Pennell D J and Firmin D N 2014 Optimal diffusion weighting for *in vivo* cardiac diffusion tensor imaging *Magn. Reson. Med.* **74** 420–30

Scott A D, Nielles-Vallespin S, Ferreira P F, McGill L A, Pennell D J and Firmin D N 2016 The effects of noise in cardiac diffusion tensor imaging and the benefits of averaging complex data *NMR Biomed.* **29** 588–99

Streeter D D 1979 Gross morphology and geometry of the heart *The Cardiovascular System* (Bathesda: American Physiology Society) pp 61–112

The Mathworks Inc. 2016 MATLAB 2015—MathWorks (www.mathworks.com/products/matlab, www.mathworks.com/products/matlab/)

Torrent-Guasp F 1973 *The Cardiac Muscle* (Madrid: Foundacion Juan March)

Toussaint N, Stoeck C T, Schaeffter T, Kozerke S, Sermesant M and Batchelor P G 2013 *In vivo* human cardiac fibre architecture estimation using shape-based diffusion tensor processing *Med. Image Anal.* **17** 1243–55

Usson Y, Parazza F, Jouk P S and Michalowicz G 1994 Method for the study of the three-dimensional orientation of the nuclei of myocardial cells in fetal human heart by means of confocal scanning laser microscopy *J. Microsc.* **174** 101–10

Weber K T 1989 Cardiac interstitium in health and disease: The fibrillar collagen network *J. Am. Coll. Cardiol.* **13** 1637–52

Wei H, Viallon M, Delattre B M A, Moulin K, Yang F, Croisille P and Zhu Y 2015 Free-breathing diffusion tensor imaging and tractography of the human heart in healthy volunteers using wavelet-based image fusion *IEEE Trans. Med. Imaging* **34** 306–16

Whittaker P, Boughner D R and Kloner R A 1989 Analysis of healing after myocardial infarction using polarized light microscopy *Am. J. Pathol.* **134** 879–93

World Medical Association 2013 World Medical Association Declaration of Helsinki. Ethical principles for medical research involving human subjects *J. Am. Med. Assoc.* **310** 2191–4

Wu M T, Tseng W Y I, Su M Y M, Liu C P, Chiou K R, Wedeen V J, Reese T G and Yang C F 2006 Diffusion tensor magnetic resonance imaging mapping the fiber architecture remodeling in human myocardium after infarction: correlation with viability and wall motion *Circulation* **114** 1036–45

Yang F, Zhu Y M, Magnin I E, Luo J H, Croisille P and Kingsley P B 2012 Feature-based interpolation of diffusion tensor fields and application to human cardiac DT-MRI *Med. Image Anal.* **16** 459–81

Yang F, Zhu Y, Luo J, Robini M, Liu J and Croisille P 2014 A comparative study of different level interpolations for improving spatial resolution in diffusion tensor imaging *IEEE J. Biomed. Heal. Inform.* **18** 1317–27

Yang F, Zhu Y, Michalowicz G, Usson Y, Fanton L, Viallon M, Clarysse P, Jouk P-S and Croisille P 2017 Validation of dMRI-derived fiber orientations using PLI in human fetal hearts *ISMRM 2017 (Honolulu, HI)* p 4769

Yang F, Zhu Y, Rapacchi S, Luo J-H, Robini M and Croisille P 2011 Interpolation of vector fields from human cardiac DT-MRI *Phys. Med. Biol.* **56** 1415–30